

## Perovskite-ion beam interactions : toward controllable light emission and lasing

Wang, Yue; Gu, Zhiyuan; Ren, Yinjuan; Wang, Ziming; Yao, Bingqing; Dong, Zhili; Adamo, Giorgio; Zeng, Haibo; Sun, Handong

2019

Wang, Y., Gu, Z., Ren, Y., Wang, Z., Yao, B., Dong, Z., . . . Sun, H. (2019). Perovskite-ion beam interactions : toward controllable light emission and lasing. *ACS Applied Materials & Interfaces*, 11(17), 15756-15763. doi:10.1021/acsami.9b01592

<https://hdl.handle.net/10356/142815>

<https://doi.org/10.1021/acsami.9b01592>

---

This document is the Accepted Manuscript version of a Published Work that appeared in final form in *ACS Applied Materials & Interfaces*, copyright © American Chemical Society after peer review and technical editing by the publisher. To access the final edited and published work see <https://doi.org/10.1021/acsami.9b01592>

*Downloaded on 20 Mar 2024 17:45:15 SGT*

## Processing all-inorganic halide perovskites for controlled light emission and lasing by focused ion beam

*Yue Wang<sup>1,2</sup>, Zhiyuan Gu<sup>2</sup>, Yinjuan Ren<sup>3</sup>, Ziming Wang<sup>1</sup>, Bingqing Yao<sup>4</sup>, Zhili Dong<sup>4</sup>, Giorgio Adamo<sup>5</sup>, Haibo Zeng<sup>1\*</sup>, Handong Sun<sup>2,5,6\*</sup>*

<sup>1</sup>MIIT Key Laboratory of Advanced Display Materials and Devices, Institute of Optoelectronics & Nanomaterials, College of Materials Science and Engineering, Nanjing University of Science and Technology, Nanjing 210094, China

<sup>2</sup>Division of Physics and Applied Physics, School of Physical and Mathematical Sciences, Nanyang Technological University, Singapore 637371, Singapore

<sup>3</sup>Department of Chemistry, National University of Singapore, 3 Science Drive 3, Singapore 117543, Singapore

<sup>4</sup>School of Materials Science and Engineering, Nanyang Technological University, Nanyang Avenue, Singapore 639798, Singapore

<sup>5</sup>Centre for Disruptive Photonic Technologies (CDPT), Nanyang Technological University, Singapore 637371, Singapore

<sup>6</sup>MajuLab, CNRS-UCA-SU-NUS-NTU International Joint Research Unit, Singapore

\* Authors to whom correspondence should be addressed, electronic email: [hdsun@ntu.edu.sg](mailto:hdsun@ntu.edu.sg); [zeng.haibo@njust.edu.cn](mailto:zeng.haibo@njust.edu.cn)

**Abstract:** All-inorganic cesium lead halide perovskites hold great promise for the development of next-generation optoelectronics. However, it remains unexplored how the energetic ions will impact CsPbX<sub>3</sub>, which may largely limit the application potentials. In this work, we for the first time investigate the interaction between the CsPbX<sub>3</sub> and high-energy gallium ions in a broad range of ion doses provided by a focused ion beam (FIB) system. We found that the optical properties of CsPbX<sub>3</sub> are highly sensitive to the energetic Ga<sup>+</sup> ions due to the relatively vulnerable ionic bonding. Specifically, even low-dose Ga<sup>+</sup> irradiation ( $\sim 1 \times 10^{15}$  ions/cm<sup>2</sup>) can lead to more than one-order-of-magnitude reduction in the photoluminescence (PL) intensity, which can be attributed to the combined effects of the formation of vacancy/interstitial defects, generation of metallic Pb-related nonradiative recombination centers and crystal-to-amorphization transition. With the increase of ion dose ( $\sim 10^{17}$  ions/cm<sup>2</sup>), the morphology of CsPbX<sub>3</sub> can be dramatically altered due to the ion sputtering effect. We demonstrate that both low- and high-dose FIB treatment can be important for realizing the application prospects of CsPbX<sub>3</sub> in optical security protection and system-on-a-chip compatible microlasers. Our results offer significant information about the ion impacts on CsPbX<sub>3</sub> and offer an enabling tool to manipulate the emission and lasing from CsPbX<sub>3</sub>, which could push ahead the potential of CsPbX<sub>3</sub> in photonics and optoelectronics.

**Keywords:** Inorganic perovskites, focused ion beam, ion-perovskite interaction, microlaser.

Organic-inorganic lead halide perovskites have been attracting intense interest by virtue of their intriguing potential in photovoltaics, light-emitting diodes (LEDs) and lasers.<sup>[1-5]</sup>

However, these organic-inorganic perovskites are notorious to degrade upon exposure to heat, oxygen and moisture, which hinders their practical applications and commercialization.<sup>[1, 4]</sup> Notably, all-inorganic cesium lead halide perovskites ( $\text{CsPbX}_3$ ,  $\text{X}=\text{Cl}$ ,  $\text{Br}$ ,  $\text{I}$ ) had been demonstrated to possess superior optical/electric properties and much enhanced stability compared to the organic-inorganic analogues, thus holding great promise for the development of next-generation optoelectronics.<sup>[6-8]</sup> Up till now, solar cells based on  $\text{CsPbI}_3$  have reached 10.77% in power conversion efficiency (PCE) and the  $\text{CsPbBr}_3$ -based LEDs have manifested a high external quantum efficiency of up to 20.3%.<sup>[9, 10]</sup>

Recently, the interaction between  $\text{CsPbX}_3$  and high-energy X-rays as well as gamma-rays ( $\gamma$ -rays) has been explored and led to the discovery of the highly sensitive nuclear radiation detectors and scintillators based on  $\text{CsPbX}_3$ .<sup>[11-13]</sup> As another high-energy radiation, energetic ions are well-known to be able to tailor the material structure and properties, resulting in a large number of important applications including microelectronics, radiotherapy treatment, and engineering of nanomaterials.<sup>[14-16]</sup> For example, dramatic enhancement of near-band-edge emission and suppression of the deep-level emission was demonstrated in  $\text{ZnO}$  by ion irradiation.<sup>[16]</sup> Moreover, energetic ions are also overwhelmingly used in semiconductor technology to introduce electrical doping in a controlled fashion and thereby tuning the electronic properties.<sup>[14]</sup>

Nowadays, the focused ion beam (FIB) technology has become mature and popular, especially in semiconductor industry, providing an enabling tool for surface modification, ion implantation, and integrated circuit repair.<sup>[14]</sup> Therefore, it is significant to gain knowledge about the impact of energetic ions on the photophysical properties for any emerging and potentially important materials in terms of both fundamental physics and practical applications.

Despite that tremendous efforts had been devoted to the research of  $\text{CsPbX}_3$  perovskites, it remains unknown how the energetic ions will impact  $\text{CsPbX}_3$ , which, otherwise, may

contribute to the improved performance and new functionalities of CsPbX<sub>3</sub>-based optoelectronic devices.<sup>[12, 17]</sup> In this work, we for the first time explore the interaction between the CsPbX<sub>3</sub> and high-energy gallium ions (Ga<sup>+</sup> ions at 30 keV) in a broad range of ion doses provided by a commercial FIB system. We found that the optical properties of CsPbX<sub>3</sub> are highly sensitive to the energetic Ga<sup>+</sup> ions due to the relatively vulnerable ionic bonding. Specifically, even low-dose Ga<sup>+</sup> irradiation ( $\sim 1 \times 10^{15}$  ions/cm<sup>2</sup>) leads to more than one-order-of-magnitude reduction in the photoluminescence (PL) intensity from CsPbBr<sub>3</sub>. According to the electronic microscopy, X-ray photoelectron spectroscopy and comprehensive optical characterizations, the PL quenching phenomenon can be attributed to the combined effects of the formation of vacancy/interstitial defects, generation of metallic Pb-related nonradiative recombination centers and crystal-to-amorphization transition. Interestingly, such spatially controllable PL fits for the microscale security protection applications and can be adopted to in-situ tune the laser emission from CsPbBr<sub>3</sub>. With the increase of ion dose ( $\sim 10^{17}$  ions/cm<sup>2</sup>), the morphology of CsPbX<sub>3</sub> can be dramatically altered due to the ion sputtering effect. By taking advantage of the mature FIB technique and optimizing the ion parameters, we demonstrate that the CsPbBr<sub>3</sub> crystals can be sculpted into precisely controlled shapes and sizes, enabling the top-down fabrication of the customizable and reproducible microlasers that are unattainable by the bottom-up synthetic routes. Our results offer essential information about the ion impacts on CsPbX<sub>3</sub> and provide a practical tool to manipulate the emission and lasing from CsPbX<sub>3</sub>, which could greatly push ahead the prospects of CsPbX<sub>3</sub> in photonic and optoelectronic applications.

The CsPbX<sub>3</sub> microcrystals with lateral dimensions of several tens to hundreds of micrometers and thickness of hundreds of nanometers were fabricated by the chemical vapor deposition method (see Experimental Section for detailed fabrication process).<sup>[18]</sup> The elemental mapping analysis by the energy dispersive X-ray spectroscopy (EDX) coupled with scanning electron microscopy (SEM) on individual CsPbBr<sub>3</sub> microplates manifests the

uniform spatial distribution of Cs, Pb, and Br and confirms the formation of CsPbBr<sub>3</sub> compound (Figure S1, Supporting Information). The X-ray diffraction (XRD) measurement reveals the cubic phase of the CsPbBr<sub>3</sub> crystals (Figure S2, Supporting Information), which is consistent with previous reports.<sup>[18, 19]</sup> The Helios 600 NanoLab FIB was employed to deliver the energetic gallium ions (Ga<sup>+</sup> at 30 keV) and the sample was placed in the SEM/FIB dual beam system consisted of both electron- and ion-columns (Figure 1a). To test the impacts of the Ga<sup>+</sup> ions on CsPbBr<sub>3</sub> microcrystals, we start with low dose ion irradiation on the sample in range of  $\sim 10^{14}$ - $10^{15}$  ions/cm<sup>2</sup>. Figure 1b shows the SEM image of the FIB-treated CsPbBr<sub>3</sub> surface. The dark squares correspond to the FIB-treated area, where the ion dose gradually increases from  $1.8 \times 10^{14}$  ions/cm<sup>2</sup> to  $1.5 \times 10^{15}$  ions/cm<sup>2</sup> with equal intervals from 1 to 8 as labelled in Figure S3, Supporting Information, and the square becomes more and more darker with the increase of ion dose. The corresponding optical image of the FIB-treated sample is presented in Figure 1c, which does not show any observable change on the surface due to the low ion dose treatment. Interestingly, the fluorescent image under laser excitation (wavelength: 442 nm) clearly manifests the FIB-treated squares as being much less emissive than the pristine parts, indicating that the PL was quenched by the ion irradiation (Figure 1d). In order to quantitatively analyze the PL change in CsPbBr<sub>3</sub> by ion irradiation, we performed the ion-dose dependent steady-state PL measurements. As shown in Figure 2a, the PL intensity keeps decreasing with the increase of ion dose and the PL intensity with ion irradiation of  $\sim 1 \times 10^{15}$  ions/cm<sup>2</sup> reduces by more than one order of magnitude (inset in Figure 2a). Simultaneously, the time-resolved PL measurement reveals that the PL decay rate rises with the increase of ion dose (Figure 2b), which suggests that more carrier trap defects are formed under higher ion dose irradiation. As the binding energy of the atoms in the CsPbBr<sub>3</sub> target sample (several eV)<sup>[20]</sup> is much smaller than the kinetic energy of Ga<sup>+</sup> ion at 30 keV, the atoms in CsPbBr<sub>3</sub> will be readily displaced from their lattice positions by the elastic core collision resulting from energy and momentum exchanges when the Ga<sup>+</sup> ion beam is directed onto the target

sample.<sup>[14, 21]</sup> Moreover, the incident ions after collision and the target atoms knocked free from the lattice sites may still have enough energy to displace more target atoms, which in turn continue to dislocate yet other atoms.<sup>[14, 22]</sup> As a result, a “displacement cascade” is formed upon  $\text{Ga}^+$  ion irradiation, which generates plenty of defects including vacancies and interstitials, leading to the PL quenching phenomenon. In general, the penetration depth of the  $\text{Ga}^+$  ion beam lies in the range of several to tens of nanometers, so that the irradiation induced quenching effects primarily occurs on the surface of sample.<sup>[14]</sup> To investigate the composition change upon  $\text{Ga}^+$  ion irradiation, we performed the surface-sensitive X-ray photoelectron spectroscopy (XPS) measurements on the  $\text{CsPbBr}_3$  sample before and after FIB treatment. The presence of Cs, Pb and Br element is consistent with the material composition of  $\text{CsPbBr}_3$  (Figure S4, Supporting Information). Whilst, upon the FIB treatment ( $1.5 \times 10^{15}$  ions/ $\text{cm}^2$ ), new peaks locating near Pb  $4f_{7/2}$  and Pb  $4f_{5/2}$  peaks were observed (Figure 2c), indicating the formation of metallic Pb ( $\text{Pb}^0$ ).<sup>[23, 24]</sup> The presence of  $\text{Pb}^0$  can effectively serve as the nonradiative recombination centers,<sup>[24]</sup> which may further contribute to the PL reduction. It is noted that we do not observe the signal related to the gallium element, indicating that gallium is not present above 0.1% concentration (the detection limit for XPS instrument) in the FIB-treated  $\text{CsPbBr}_3$  surface.<sup>[25]</sup>

We also performed the transmission electron microscopy (TEM) to access the change of crystal structure by the  $\text{Ga}^+$  ion irradiation. To do so, we scratched the  $\text{CsPbBr}_3$  microcrystals and collected the tiny fragments onto the copper grids. Afterwards, the edge of the  $\text{CsPbBr}_3$  fragment was treated by FIB ( $1.5 \times 10^{15}$  ions/ $\text{cm}^2$ ) and then examined by TEM. As displayed in Figure 2e, clear lattice fringes can be observed for the  $\text{CsPbBr}_3$  fragment before FIB treatment, indicating the high crystalline nature. Whilst, many nanometer-sized particles are formed and the lattice fringes disappear after the FIB treatment, indicating that the ion irradiation can induce the transition from crystal to amorphous phase.

As a result of the high energy of  $\text{Ga}^+$  ions, some of the target atoms can be ejected from the surface of the sample, the process is known as ion sputtering.<sup>[14]</sup> Notably, the surface morphology of the  $\text{CsPbBr}_3$  sample can be dramatically transformed due to ion sputtering effect. Figure 2d shows the atomic force microscopy (AFM) image of  $\text{CsPbBr}_3$  after FIB treatment with relatively low ion dose ( $2.5 \times 10^{14}$  ions/ $\text{cm}^2$ ). It is found that the concave square with depth of  $\sim 5$  nm was formed. Deeper concave with microscale depth can be obtained by the higher-dose FIB treatment. Figure 1b displays the SEM image of the representative deep concave square fabricated by high-dose FIB treatment ( $1.25 \times 10^{17}$  ions/ $\text{cm}^2$ ) as numbered “0”. In the following part, we will show that the high-dose FIB treatment can be adopted as an enabling tool to sculpt the  $\text{CsPbBr}_3$  into microlasers with on-demand resonators so as to overcome the limitations of the  $\text{CsPbX}_3$ -microlasers made from the bottom-up approach.

The ability to spatially control the emission from  $\text{CsPbX}_3$  in a programmable manner allows the potential applications in security protection ranging from the information encryption to anticounterfeiting.<sup>[26, 27]</sup> Quick response (QR) Code is a 2D matrix code that contains a high capacity as the dot-based 2D binary code scheme can provide a higher density of binary code information than a line-based 1D barcode scheme.<sup>[27]</sup> As a proof-of-concept experiment, we designed a QR Code whose mirror image corresponds to the text “perovskite” and then duplicated it on  $\text{CsPbBr}_3$  microcrystals by low-dose FIB treatment (see the SEM image in Figure 3g). Figure 3a shows the optical image of the  $\text{CsPbBr}_3$  microcrystals under microscope and the QR Code is invisible due to small topographical modification (thickness contrast:  $< 10$  nm) of the surface by the low-dose ion treatment ( $2.5 \times 10^{14}$  ions/ $\text{cm}^2$ ). It is worth noting that the realization of photopatterns without notably changing the morphology renders an ideal security-protection strategy. When the  $\text{CsPbBr}_3$  microcrystals are exposed to the laser excitation, the QR Code emerges (Figure 3d). The size of the QR Code can be easily controlled by the FIB technique as demonstrated in Figs. 3d, e and f. By virtue of the high



photo-emissive property of  $\text{CsPbBr}_3$ , a feature that makes  $\text{CsPbBr}_3$  attractive in light-emitting applications, and the favorable PL contrast induced by ion irradiation, the QR Code is readily observable by the cheap and commercially available lamps as demonstrated in Figures S5, where the QR is well decoded by a Xenon lamp ( $\sim 10 \text{ mW/cm}^2$ ) in combination with a band pass filter (390-420 nm). Moreover, leveraging on the facile emission wavelength tunability of  $\text{CsPbX}_3$  by tailoring the composition, the blue and red QR Code (Figure S6, Supporting Information) can be made based on the  $\text{CsPb}(\text{Cl}/\text{Br})_3$  and  $\text{CsPb}(\text{Br}/\text{I})_3$ , respectively.

Besides the QR Code, the text information can also be encoded by simply pre-defining it in the FIB system. As an example, the word “encryption” was written on the  $\text{CsPbBr}_3$  sample and the word was clearly resolved by the laser excitation (Figure 3h). It is well-known that FIB can reach nanometer spatial resolution, thus patterns or texts with subwavelength scale can be encrypted. Figure 3i shows the stripes fabricated by FIB treatment, it is found that the width of the stripe can be made as small as several tens of nanometers, making the subwavelength encryption feasible. Figure 3j shows the code “0101” in nanometer scale written on the sample (see Figure S7 for large-area SEM image, Supporting Information). Noting that the code with such tiny dimension cannot be distinguished by the common optical imaging system due to the diffraction limit. Nevertheless, the more advanced imaging techniques, such as the scanning near-field optical microscopy (SNOM),<sup>[28]</sup> may be feasible for the decryption.

In addition to being excellent for spontaneous emission,  $\text{CsPbX}_3$  perovskites have also been recognized as superior laser materials because of the large absorption coefficient and defect-tolerant nature.<sup>[7, 29-32]</sup> Inspired by the effective PL quenching in  $\text{CsPbX}_3$ , we speculate that lasing emission from  $\text{CsPbX}_3$  could be manipulated by purposely introducing optical loss via selective FIB treatment, which would be not only interesting for fundamental research but also important for practical applications. To confirm the hypothesis, we adopt the cubic  $\text{CsPbBr}_3$  microplate which had been demonstrated to serve as favorable microlasers<sup>[19, 33]</sup> as

the model system. Figure 4g shows the pump-fluence dependent micro-PL ( $\mu$ -PL) spectra from the individual  $\text{CsPbBr}_3$  microplate (see details of  $\mu$ -PL measurement in Experimental Section). Under relatively low pump fluence ( $< \sim 16.0 \mu\text{J cm}^{-2}$ ), the PL is dominated by a broad emission band with full-width at half maximum (FWHM) of  $\sim 20$  nm peaking at  $\sim 528$  nm. With the increase of pump fluence, evenly-spaced spikes appear. The plot of the integrated intensity over the sharp peak spectral range as a function of the pump fluence exhibits a super-linear behavior (inset in Figure 4g), indicating the achievement of lasing action with low threshold ( $P_{\text{th}}$ ) of  $\sim 16.0 \mu\text{J cm}^{-2}$ .<sup>[34]</sup> The fluorescent image of  $\text{CsPbBr}_3$  microplate exhibits nearly uniform green emission when the excitation fluence is below threshold (Figure 4a). While, a bright periphery of the microplate is observed as the pump fluence exceeds the threshold (Figure 4b), indicating the whispering gallery mode (WGM) lasing occurred in the perovskite microplates.<sup>[35]</sup> In the cubic WGM cavity, the free spectral range ( $FSR$ ) is given by:  $FSR = \frac{\lambda^2}{2\sqrt{2}Ln_g}$ ,<sup>[34]</sup> where  $\lambda$  is the lasing wavelength and  $L$  is the edge length of the microplate. Accordingly, the group refractive index  $n_g$  is derived to be  $\sim 4.2$ , which agrees well with previous reports.<sup>[19]</sup> In fact, it is not surprising to observe WGM lasing from the  $\text{CsPbBr}_3$  microplates since the cubic microcrystal naturally behaves as the high-Q WGM resonator.<sup>[19, 33, 34]</sup> To demonstrate the feasibility of lasing manipulation by FIB, we partially treat the perovskite microplate by  $\text{Ga}^+$  ion irradiation with low dose of  $\sim 3 \times 10^{15}$  ions/ $\text{cm}^2$ . As shown in Figure 4d, the fluorescent image of the perovskite microplate under low excitation fluence ( $\sim 5 \mu\text{J cm}^{-2}$ ) exhibits obvious PL quenching phenomenon in the FIB-treated area. The corresponding  $\mu$ -PL spectra from the FIB-treated microplate are presented in Figure 4h. Similarly, the PL spectra are dominated by the broad spontaneous emission under relatively low pump fluence ( $< \sim 24 \mu\text{J cm}^{-2}$ ). As pump fluence further increases, sharp spikes emerge, and the plot of the integrated PL intensity over pump fluence exhibits the threshold-

like behavior, which suggests the occurrence of lasing action in the FIB-treated CsPbBr<sub>3</sub> microplate. Notably, in sharp contrast to the pristine CsPbBr<sub>3</sub> microplate, only a pair of bright edges in the untreated area were observed for the FIB-treated microplate (Figure 4e), which indicates the development of Fabry–Pérot (F-P) lasing instead of WGM lasing. By taking the measured *FSR* of 1.33 nm into the formula describing F-P oscillation:  $FSR = \frac{\lambda^2}{2Ln_g}$ , the group refractive index is derived to be ~4.1, further confirming the F-P lasing mechanism in the FIB-treated microplate. In principle, as a result of the optical loss induced by the FIB treatment, the CsPbBr<sub>3</sub> microplate fails to provide sufficient optical gain for WGM oscillation, thereby leading to the transition from WGM to F-P lasing in the FIB-treated microplate. The corresponding resonant oscillations in the pristine and FIB-treated CsPbBr<sub>3</sub> microplate can be well retrieved by numerical simulation using finite element method (FEM) (see details in Experimental Section) as shown in Figures 4c and 4f, respectively.

Till now, almost all of CsPbX<sub>3</sub>-based microlasers are developed from the bottom-up method.<sup>[19, 32]</sup> However, the bottom-up growth of the CsPbX<sub>3</sub> microcrystals lacks the controllability of the crystal size and shape.<sup>[31]</sup> Thus, the lasing characteristics of one particular CsPbX<sub>3</sub>-microlaser are difficult to duplicate in another, which fails to meet the demands of on-chip integrated photonic applications. Moreover, these as-grown microcrystals have limited morphologies, such as the triangles, squares, and hexagons,<sup>[19, 31, 32]</sup> which restricts the diversity and potential of CsPbX<sub>3</sub>-based microlasers. As shown above, the high-dose ion irradiation could dramatically alter the morphology of the perovskites, such finding triggers us to explore the fabrication of CsPbX<sub>3</sub> microlasers by top-down approach via FIB treatment, aiming at overcoming the limitations of the bottom-up produced CsPbX<sub>3</sub> microlasers. Figure 5b shows the typical SEM image of the microdisk fabricated by high-dose FIB sputtering ( $1.25 \times 10^{17}$  ions/cm<sup>2</sup>). By optimizing the parameters including current (22 pA), beam diameter (15 nm) and ion incident angle (90°), smooth surface of the perovskite

microdisks can be obtained (Figure S8, Supporting Information). It is known that the smooth surface can reduce the optical loss and enable the high-Q microcavities.<sup>[36]</sup> Moreover, the vertical incidence of ions onto the sample can suppress the ion-induced optical loss on the surface, thus the bright green-color microdisk (Figure S9, Supporting Information) can be observed under low excitation fluence ( $\sim 5 \mu\text{J cm}^{-2}$ ). To check the lasing performance, we performed the pump-fluence dependent  $\mu$ -PL measurement from the individual microdisk. Figure 5a shows the  $\mu$ -PL spectra from a typical microdisk with diameter of  $27.1 \mu\text{m}$  (Figure 5c for the SEM image). Again, the PL spectra are dominated by the broad spontaneous emission under low excitation intensities ( $< \sim 20 \mu\text{J cm}^{-2}$ ). As the pump fluence keeps increasing, evenly-spaced sharp peaks appear, and the plot of the integrated PL intensity over pump fluence exhibits nonlinear behavior (inset in Figure 5a), indicating the development of lasing action in the  $\text{CsPbBr}_3$  microdisk. To get deeper insights, we carried out the time-resolved  $\mu$ -PL measurements on the individual  $\text{CsPbBr}_3$  microdisk with different excitation fluences (Figure 5i). It is seen that the spontaneous emission lifetime is  $\sim 460$  ps at low pump fluence ( $\sim 0.2 P_{\text{th}}$ ). As the pump fluence increase to  $\sim 0.8 P_{\text{th}}$ , the lifetime decreases to  $\sim 240$  ps. Notably, when the pump fluence exceeds the threshold ( $\sim 1.2 P_{\text{th}}$ ), a much faster decay channel with lifetime of  $< \sim 50$  ps (limited by the temporal response of the streak camera system) is revealed, which corresponds to the stimulated emission process and further confirms the occurrence of lasing action. To the best of our knowledge, it represents the first report of the laser emission from circular-shaped  $\text{CsPbBr}_3$  microdisk.

The corresponding fluorescent image of the  $\text{CsPbBr}_3$  microdisk above lasing threshold (Figure 5f) exhibits bright ring around the periphery, which suggests the WGM lasing mechanism. Hence, we tentatively examined the lasing peaks using WGM model. Considering the first radial mode order ( $q = 1$ ), the resonant condition is given by:  $m\lambda_m = \pi n_g D$ , where  $m$  and  $\lambda_m$  are the angular mode number and the resonant wavelength at

$m$ , respectively, and  $D$  is the diameter of the microdisk. Following the procedure reported by Ta et al.,<sup>[35]</sup> the lasing peaks are found to match well with the mode numbers indexed as 756–763 (Figure S10a, Supporting Information). The Q-factor (calculated by  $Q = \lambda/\Delta\lambda$ , where  $\lambda$  and  $\Delta\lambda$  are the lasing peak wavelength and the corresponding linewidth of the lasing peak, respectively) is derived to be as high as  $\sim 2700$ . The resonances in circular-shaped microdisks can be retrieved via numerical studies as shown in the inset of Figure 5h and the electric field is found to be effectively confined close to the inner boundary of CsPbBr<sub>3</sub> microdisk (Figure 5h), which is beneficial for the development of high-Q laser emission.<sup>[37]</sup>

By means of the mature FIB technology, the top-down fabricated perovskite microlasers are highly reproducible and controllable. Figure S11 shows the lasing spectra from another FIB-fabricated 27.1  $\mu\text{m}$ -sized CsPbBr<sub>3</sub> microdisk. It is found that the lasing wavelength,  $FSR$  and Q-factor are nearly the same as those of the one shown in Figure 5a, indicating that the lasing characteristics can be duplicated by the FIB approach, which is essential for applications including on-chip integrated optoelectronics. The size of CsPbBr<sub>3</sub> microdisks can be readily manipulated by FIB method. Figures 5b, c and d display the SEM images of CsPbBr<sub>3</sub> microdisks with different sizes and the corresponding lasing images are shown in Figures 5e (Diameter: 30.2  $\mu\text{m}$ ), f (Diameter: 27.1  $\mu\text{m}$ ) and g (Diameter: 5.0  $\mu\text{m}$ ), respectively. The size dependent lasing spectra disclose that the  $FSR$  increases with the decrease of the microdisk diameter (Figure S10b, Supporting Information), which agrees with WGM lasing behavior.<sup>[37, 38]</sup> Besides, other resonator shapes, such as the deformed CsPbBr<sub>3</sub> microdisk (Figure S12, Supporting Information), can also be fabricated and the lasing emission with nonuniform angular distribution is achieved, which provides an excellent platform to explore light-matter interaction in customizable laser resonators.

In summary, we investigated the interaction between CsPbX<sub>3</sub> and high-energy gallium ions (Ga<sup>+</sup> ions at 30 keV) in a broad range of ion doses for the first time. We revealed that both low-dose ( $\sim 10^{14}$  ions/cm<sup>2</sup>) and high-dose ( $\sim 10^{17}$  ions/cm<sup>2</sup>) ion irradiations can serve as

effective tools to manipulate the light emission and lasing from  $\text{CsPbX}_3$  and the underlying physical mechanisms are provided. Our results represent a significant step towards applying the emerging  $\text{CsPbX}_3$  for photonic applications.

## Experimental Section

*Synthesis of  $\text{CsPbX}_3$  microcrystals:* The  $\text{CsPbX}_3$  microcrystals were fabricated by the chemical vapor deposition method. The ITO-glass substrate was placed inside the downstream of quartz tube in Ar atmosphere. The precursor was prepared by mixing powder of  $\text{PbX}_2$  and CsBr with molar ratio of 1:1. The reaction temperature was set at 575 °C and hold for 15 min. The  $\text{CsPbX}_3$  microcrystals with lateral dimensions of several tens to hundreds of micrometers and thickness of hundreds of nanometers can be fabricated.

*FIB treating on  $\text{CsPbX}_3$  microcrystals:* The Helios 600 NanoLab FIB was adopted to deliver gallium ions ( $\text{Ga}^+$  at 30 keV) and the  $\text{CsPbX}_3$  sample was placed in the SEM/FIB dual beam system that consisted of both electron- and ion-columns. The stage has five degrees of freedom for movement (X, Y, Z, rotation, tilt). The currents used were 22 pA.

*Optical characterization:* For the  $\mu$ -PL measurement, the sample was pumped at 400 nm by frequency-doubling of the fundamental wavelength (800 nm) from the Ti: sapphire regenerative amplifier with pulsewidth of 100 fs. The laser beam is focused to cover the whole sample by a microscope objective and the PL signal is collected by the same objective and then analyzed by a charge coupled device (CCD). For the time-resolved PL, the same laser source is adopted to excite the sample and the PL signal is recorded by an Optronis streak camera with an optimized temporal resolution of ~50 ps.

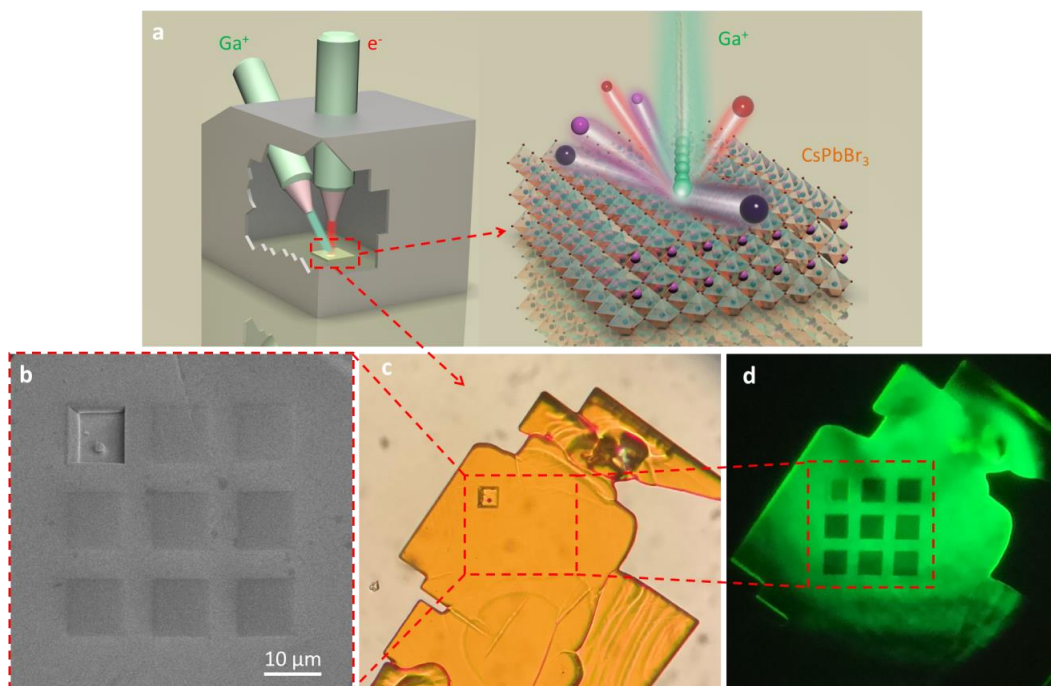


**Figure 1.** a) Schematic illustration of FIB treatment on CsPbBr<sub>3</sub> microcrystals. b) SEM image of the FIB-treated CsPbBr<sub>3</sub> microcrystal. The dark squares correspond to the FIB treated area. c) Fluorescent image of the FIB-treated CsPbBr<sub>3</sub> microcrystal. The dark squares correspond to the FIB treated area.

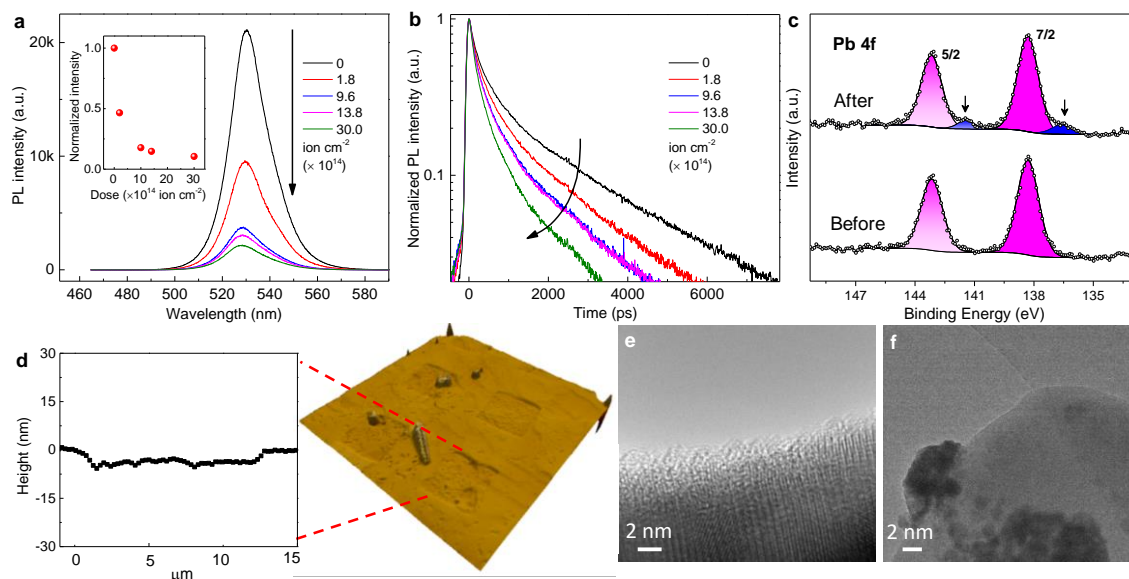


**Figure 2.** a) PL spectra from CsPbBr<sub>3</sub> with different ion dose irradiation. The inset shows the corresponding ion dose dependent integrated PL intensity from CsPbBr<sub>3</sub>. b) PL decay from CsPbBr<sub>3</sub> with different ion dose irradiation. c) XPS signals corresponding to Pb 4f before and after FIB treatment. d) Atomic force microscopy (AFM) image and the corresponding cross-section line of CsPbBr<sub>3</sub> surface with FIB treatment. e) and f) Transmission electron microscopy (TEM) of CsPbBr<sub>3</sub> fragment before and after FIB treatment.



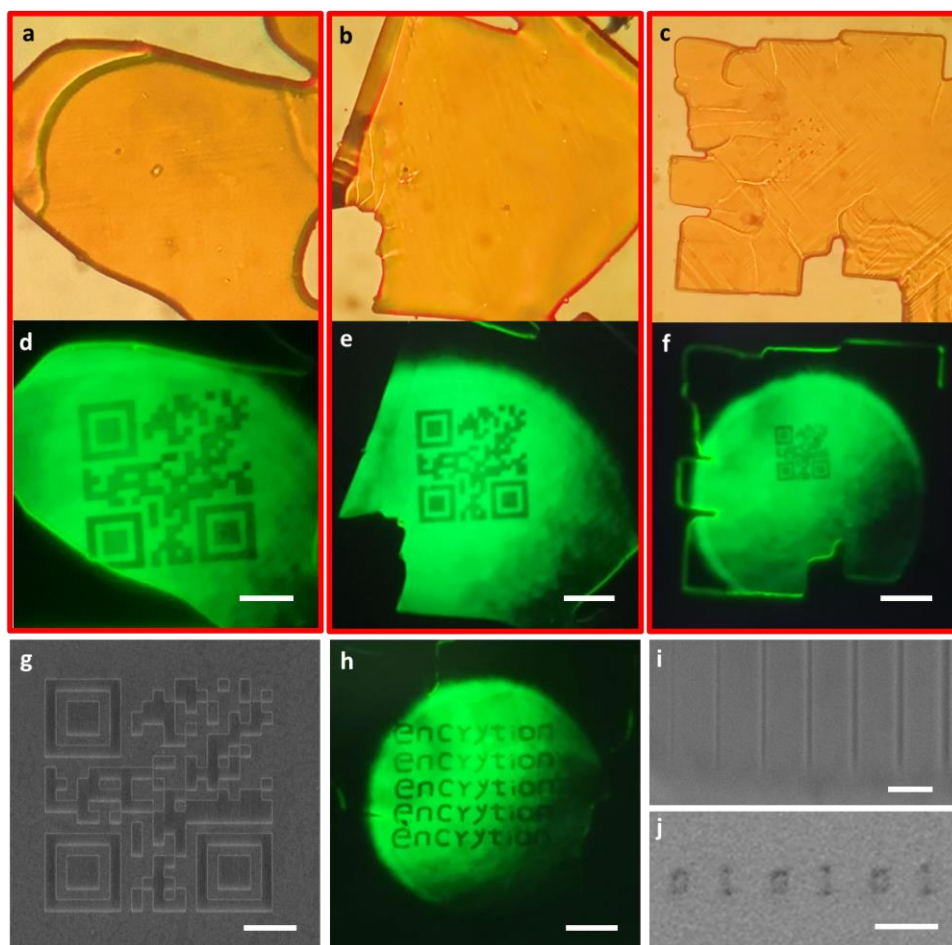


**Figure 3.** a-c) Optical images of the FIB-treated CsPbBr<sub>3</sub> microcrystal with QR Code encoding. d-f) Fluorescent images of the FIB-treated CsPbBr<sub>3</sub> microcrystal, revealing the encoded QR Code. Scale bar: 20  $\mu$ m. g) SEM image of QR Code encoded on CsPbBr<sub>3</sub> by FIB-treatment. Scale bar: 5  $\mu$ m. h) Fluorescent image of the the FIB-treated CsPbBr<sub>3</sub> microcrystal, revealing the encoded text information. Scale bar: 20  $\mu$ m. i) SEM image of stripes made by FIB treatment. Scale bar: 2  $\mu$ m. j) Nanometer sized characters (0101) encoded on CsPbBr<sub>3</sub> by FIB treatment. Scale bar: 1  $\mu$ m.

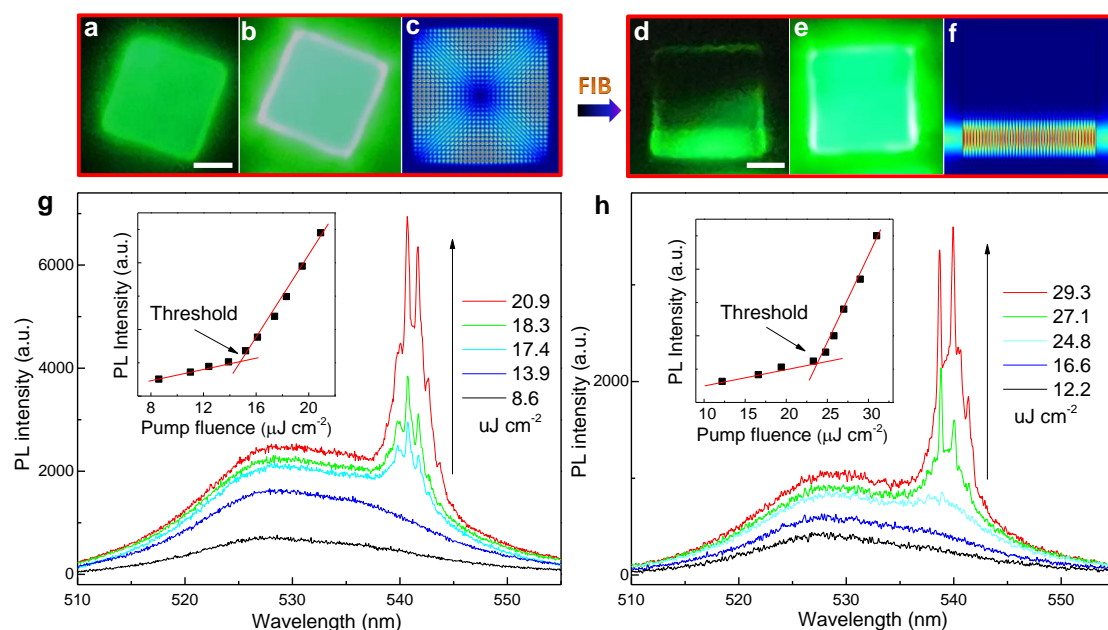


**Figure 4.** a) Below-threshold fluorescent image of the CsPbBr<sub>3</sub> microplate. Scale bar : 10  $\mu\text{m}$ . b) Above-threshold fluorescent image of the CsPbBr<sub>3</sub> microplate. c) Simulated electric field distribution inside the square perovskite cavity. d) Below-threshold fluorescent image of the FIB-treated CsPbBr<sub>3</sub> microplate. Scale bar: 10  $\mu\text{m}$ . e) Above-threshold fluorescent image of the FIB-treated CsPbBr<sub>3</sub> microplate. f) Simulated electric field distribution inside the FIB-treated perovskite cavity. g) Pump-fluence dependent PL spectra from the CsPbBr<sub>3</sub> microplate. The inset shows the integrated PL intensity over the sharp peak spectral range as a function of pump fluence. h) Pump-fluence dependent PL spectra from the FIB-treated CsPbBr<sub>3</sub> microplate. The inset shows the integrated PL intensity over the sharp peak spectral range as a function of pump fluence.

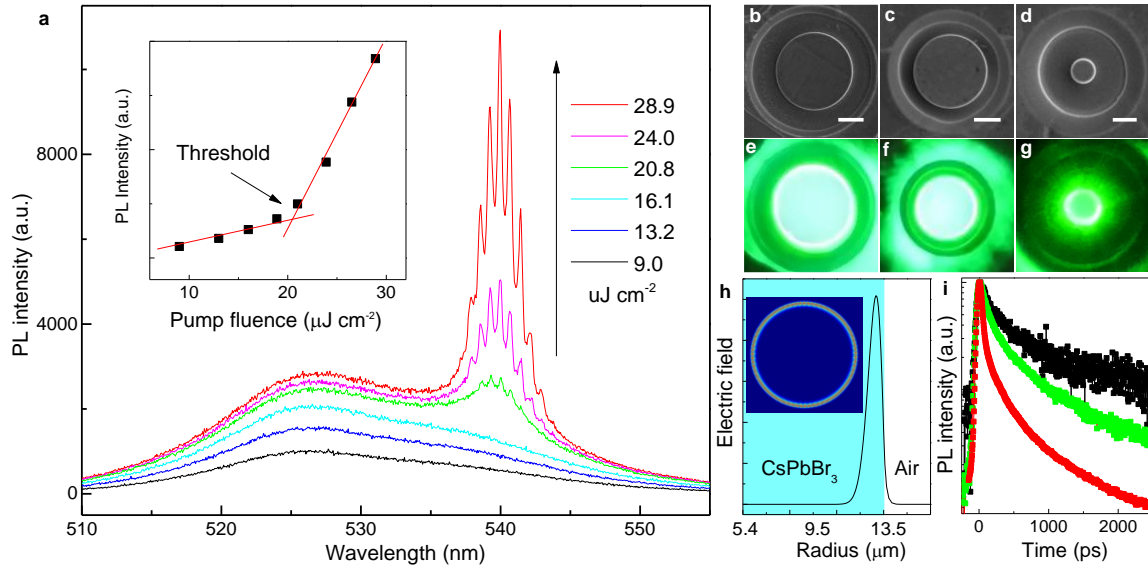


**Figure 5.** a) Pump-fluence dependent PL spectra from individual  $\text{CsPbBr}_3$  microdisk with diameter of  $27.1 \mu\text{m}$ . The inset shows the integrated PL intensity over the sharp peak spectral range as a function of pump fluence. b-d) SEM images of  $\text{CsPbBr}_3$  microdisks with diameter of b)  $30.2 \mu\text{m}$ , c)  $27.1 \mu\text{m}$  and d)  $5.0 \mu\text{m}$ . Scale bar: b)  $10 \mu\text{m}$ , c)  $10 \mu\text{m}$ , d)  $5 \mu\text{m}$ . The corresponding above-threshold fluorescent images of the microdisks are shown in e-g). h) 2D plot of the electric field distribution near the edge of the microdisk. The inset shows the electric field distribution inside the microdisk. i) Pump fluence dependent PL decay from individual  $\text{CsPbBr}_3$  microdisk with diameter of  $27.1 \mu\text{m}$ .

## References

- [1] B.R. Sutherland, E.H. Sargent, *Nature Photonics*, **2016** 10 295.
- [2] X. Yang, X. Zhang, J. Deng, Z. Chu, Q. Jiang, J. Meng, P. Wang, L. Zhang, Z. Yin, J. You, *Nature Communications*, **2018** 9 570.
- [3] W. Zhang, L. Peng, J. Liu, A. Tang, J.-S. Hu, J. Yao, Y.S. Zhao, *Advanced Materials*, **2016** 28 4040-4046.
- [4] G. Xing, N. Mathews, S.S. Lim, N. Yantara, X. Liu, D. Sabba, M. Grätzel, S. Mhaisalkar, T.C. Sum, *Nature Materials*, **2014** 13 476.
- [5] N. Zhang, W. Sun, S.P. Rodrigues, K. Wang, Z. Gu, S. Wang, W. Cai, S. Xiao, Q. Song, *Advanced Materials*, **2017** 29 1606205.
- [6] M.V. Kovalenko, L. Protesescu, M.I. Bodnarchuk, *Science*, **2017** 358 745-750.
- [7] Y. Wang, H. Sun, *Small Methods*, **2018** 2 1700252.
- [8] Y. Wang, X. Li, J. Song, L. Xiao, H. Zeng, H. Sun, *Advanced Materials*, **2015** 27 7101-7108.
- [9] K. Lin, J. Xing, L.N. Quan, F.P.G. de Arquer, X. Gong, J. Lu, L. Xie, W. Zhao, D. Zhang, C. Yan, W. Li, X. Liu, Y. Lu, J. Kirman, E.H. Sargent, Q. Xiong, Z. Wei, *Nature*, **2018** 562 245-248.
- [10] A. Swarnkar, A.R. Marshall, E.M. Sanehira, B.D. Chernomordik, D.T. Moore, J.A. Christians, T. Chakrabarti, J.M. Luther, *Science*, **2016** 354 92-95.
- [11] Y. He, L. Matei, H.J. Jung, K.M. McCall, M. Chen, C.C. Stoumpos, Z. Liu, J.A. Peters, D.Y. Chung, B.W. Wessels, M.R. Wasielewski, V.P. Dravid, A. Burger, M.G. Kanatzidis, *Nature Communications*, **2018** 9 1609.
- [12] Q. Chen, J. Wu, X. Ou, B. Huang, J. Almutlaq, A.A. Zhumeckenov, X. Guan, S. Han, L. Liang, Z. Yi, J. Li, X. Xie, Y. Wang, Y. Li, D. Fan, D.B.L. Teh, A.H. All, O.F. Mohammed, O.M. Bakr, T. Wu, M. Bettinelli, H. Yang, W. Huang, X. Liu, *Nature*, **2018** 561 88-93.
- [13] J.H. Heo, D.H. Shin, J.K. Park, D.H. Kim, S.J. Lee, S.H. Im, *Advanced Materials*, **2018** 30 1801743.
- [14] N.M. M Nastasi, J Mayer, JK Hirvonen, M James *Cambridge Univ. Press, Cambridge*, **1996**.
- [15] R.M. Papaléo, R. Thomaz, L.I. Gutierrez, V.M. de Menezes, D. Severin, C. Trautmann, D. Tramontina, E.M. Bringa, P.L. Grande, *Physical Review Letters*, **2015** 114 118302.
- [16] B. Yadian, R. Chen, H. Liu, H. Sun, Q. Liu, C.L. Gan, Z. Kun, C. Zhao, B. Zhu, Y. Huang, *Nano Research*, **2015** 8 1857-1864.
- [17] Y. Wang, X. Li, V. Nalla, H. Zeng, H. Sun, *Advanced Functional Materials*, **2017** 27 1605088-n/a.
- [18] C. Huo, X. Liu, X. Song, Z. Wang, H. Zeng, *The Journal of Physical Chemistry Letters*, **2017** 8 4785-4792.
- [19] Q. Zhang, R. Su, X. Liu, J. Xing, T.C. Sum, Q. Xiong, *Advanced Functional Materials*, **2016** 26 6238-6245.
- [20] A. Varadwaj, P.R. Varadwaj, K. Yamashita, *ChemSusChem*, **2018** 11 449-463.
- [21] J. Gierak, *Nanofabrication* 2014.
- [22] G.V. Voznyuk, I.V. Levitskii, M.I. Mitrofanov, D.N. Nikolaev, V.P. Evtikhiev, *Journal of Physics: Conference Series*, **2018** 1038 012080.
- [23] L. Zhang, X. Yang, Q. Jiang, P. Wang, Z. Yin, X. Zhang, H. Tan, Y. Yang, M. Wei, B.R. Sutherland, E.H. Sargent, J. You, *Nature Communications*, **2017** 8 15640.
- [24] W. Zhang, S. Pathak, N. Sakai, T. Stergiopoulos, P.K. Nayak, N.K. Noel, A.A. Haghighirad, V.M. Burlakov, D.W. deQuilettes, A. Sadhanala, W. Li, L. Wang, D.S. Ginger, R.H. Friend, H.J. Snaith, *Nature Communications*, **2015** 6 10030.
- [25] Y. Ren, K. Yuan, X. Zhou, H. Sun, K. Wu, S.L. Bernasek, W. Chen, G.Q. Xu, *Chemistry – A European Journal*, **0**.
- [26] Y. Wang, X. Li, S. Sreejith, F. Cao, Z. Wang, M.C. Stuparu, H. Zeng, H. Sun, *Advanced Materials*, **2016** 28 10637-10643.
- [27] R. Arppe, T.J. Sørensen, *Nature Reviews Chemistry*, **2017** 1 0031.
- [28] E. Betzig, R.J. Chichester, *Science*, **1993** 262 1422-1425.
- [29] Y. Wang, X. Li, X. Zhao, L. Xiao, H. Zeng, H. Sun, *Nano Letters*, **2016** 16 448-453.
- [30] Y. Wang, D. Yu, Z. Wang, X. Li, X. Chen, V. Nalla, H. Zeng, H. Sun, *Small*, **2017** 13 1701587-n/a.

- [31] H. Zhou, S. Yuan, X. Wang, T. Xu, X. Wang, H. Li, W. Zheng, P. Fan, Y. Li, L. Sun, A. Pan, *ACS Nano*, **2017** *11* 1189-1195.
- [32] S.W. Eaton, M. Lai, N.A. Gibson, A.B. Wong, L. Dou, J. Ma, L.-W. Wang, S.R. Leone, P. Yang, *Proceedings of the National Academy of Sciences*, **2016** *113* 1993-1998.
- [33] X. He, P. Liu, H. Zhang, Q. Liao, J. Yao, H. Fu, *Advanced Materials*, **2017** *29* 1604510.
- [34] A.K. Bhowmik, *Appl. Opt.*, **2000** *39* 3071-3075.
- [35] V.D. Ta, R. Chen, H.D. Sun, *Advanced Materials*, **2012** *24* OP60-OP64.
- [36] S.-J. Tang, S. Liu, X.-C. Yu, Q. Song, Q. Gong, Y.-F. Xiao, *Advanced Materials*, **2018** *30* 1800262.
- [37] Y. Wang, K.S. Leck, V.D. Ta, R. Chen, V. Nalla, Y. Gao, T. He, H.V. Demir, H. Sun, *Advanced Materials*, **2015** *27* 169-175.
- [38] Y. Wang, K.E. Fong, S. Yang, Van D. Ta, Y. Gao, Z. Wang, V. Nalla, H.V. Demir, H. Sun, *Laser & Photonics Reviews*, **2015** *9* 507-516.